Ceramics International 50 (2024) 54707–54715

Contents lists available at ScienceDirect

Ceramics International

journal homepage: www.elsevier.com/locate/ceramint

Synthesis of CuO/Fe_3O_4 Nanocomposite for enhanced solar thermal desalination

S.S. Fouad [a], M. Nabil [b,*], F. Horia [b], K. Easawi [b], S. Negm [b]

[a] Department of Physics, Faculty of Education, Ain Shams University, Cairo, 11566, Egypt
[b] Department of Basic Engineering Sciences, Faculty of Engineering (Shoubra), Benha University, Cairo, Egypt

ARTICLE INFO

Handling Editor: Dr P. Vincenzini

Keywords:
CuO nanoparticles
Magnetic nanoparticles
Nanocomposite
Photoacoustic spectroscopy
Water desalination

ABSTRACT

Nanoparticle (NPs) have attracted the attention of scientists and researchers in water remediation due to the improvement in its processability, and its cost effectiveness. The present work analyzed the synergistic effect of CuO (NPs) with different ratios (0, 0.5, 0.6, 0.7, 0.8, 0.9 and 1 wt %) on the structural, and optical properties of Fe_3O_4 (NPs), that can be used in water desalination process. The general methodology for preparation and structural properties of CuO (NPs), Fe_3O_4 (NPs) and CuO/Fe_3O_4 (NCs) were analyzed by (XRD) and (TEM) measurements. The morphological combination of (SEM) with (EDX), were used for determining the elemental identification of CuO/Fe_3O_4 (NCs). The characterization topography was found to be strongly affected by the change of the CuO concentration. Furthermore, the Urbach energy (E_U), steepness parameter (σ), electron-phonon interaction ($E_{e\text{-}p}$), optical band gap (E_g), refractive index (n) and optical conductivity (σ_{opt}) were calculated. The optical absorption studies in the UV–Visible region, revealed that the CuO/Fe_3O_4 (NCs) was found to be direct allowed transition, and the energy bandgap value decreased from 2.52 eV to 2.15 eV based on the percentage change of CuO (NPs) in CuO/Fe_3O_4 (NCs). Moreover, the value of thermal conductivity (k), and thermal efficiency (η), showed an increase with the increase of the ratio of CuO (NPs), which may be an indication for opening an innovation way that can satisfy the need of seawater desalination technology.

1. Introduction

Nanomaterials are promising materials that have attracted much attention because of their special characteristics in optical and electrical properties, high chemical stability and high adsorption capacity that can be used in water desalination [1–4]. Water Desalination technology has become more relevant for the use of water resources [5–8]. Desalination is the process that applied to seawater for human consumption or agricultural purposes. The most major types of technologies that are used today around the world for desalination can be broadly classified either thermal or membrane. Both technologies still require a lot of electricity and energy to extract the salts and produce fresh water. Within those two broad types, there are other different techniques. Desalination processes also generate brine, a highly concentrated and salty waste product. Today there are many solar thermal desalination water production facilities around the world of much large scale based on physical principles. Technology has become a promising option for developing nano sized particles in fluids. Nano fluids have great potential to improve the efficiency of heat transfer behavior of the conventional heat-transfer fluids [9,10]. Magnetite (Fe_3O_4) nanoparticles (NPs) have granted a lot of interest, because its properties may provide new applications in several fields [11,12]. Moreover, in photo-thermal applications, Fe_3O_4 NPs has recently attracted a lot of researcher's attention by showing its extensive photon absorption cross-section, and strong intermolecular bonds [13–15]. Furthermore, the Fe_3O_4 NPs have become an essential option for use in thermal energy conversion systems, where NPs are mixed in transparent base fluids to form nanofluids, and recently it had been successfully used for the desalination of brackish water. The oxides of transition metals have also generated excitement for its applications in magnetic storage media, solar energy transformation, electronics, and catalysis [16–27]. For this purpose, copper oxide nanoparticles CuO (NPs) has been chosen, as an interesting candidate that has a good electrical conduction, small energy gap, great chemical and physical stability and its efficiency as nanofluids in heat transfer application [28]. The CuO (NPs) has an opern shell with a direct band gap (1.2 eV) of charge -transfer type, which can absorb light up to the near infrared region, that can greatly harvest visible light, low toxicity, and easy preparation. The low-cost of CuO gained large

* Corresponding author.
E-mail address: mohammed_diab35@yahoo.com (M. Nabil).

https://doi.org/10.1016/j.ceramint.2024.10.329
Received 19 March 2024; Received in revised form 21 October 2024; Accepted 22 October 2024
Available online 22 October 2024
0272-8842/Published by Elsevier Ltd.

interest because of their potential towards diversified application, such as adsorption properties. Therefore, several research investigated the physicochemical properties of the combination of Fe_3O_4 (NP_S) with CuO (NPs) and its applications are important [29]. Copper oxide is reduced to copper by the iron (reduction is removal of oxygen, at this level) without given any toxic vapours. Also, the efficient adsorption of the above-mentioned nanocomposites with high separation ability from any solution have a very good potential and high adsorption efficiency against wide range of frequency used toxic industrial techniques for use in water remediation [30]. We reported on CuO/Fe_3O_4 composite that featured higher adsorption compared to Fe_3O_4. Meanwhile, the low cost, easy synthesis and super paramagnetic properties make these affordable and reusable materials. The low cost copper-based metal oxides (CuO) are also gaining large interest because of their potential towards diversified applications [30]. In this study, CuO/Fe_3O_4 (NCs) was successfully prepared with different percentages of CuO (NPs) (0, 0.5, 0.6, 0.7, 0.8, 0.9, 1 wt%), and then their physicochemical properties were investigated using XRD, SEM-EDX, TEM. Among all the available wastewater treatment techniques, by using the adsorption approach due to its effectiveness, economy and simplicity, the absorption and transmittance spectra of seven different NCs samples were investigated under different experimental techniques were used. The thermal parameters for the prepared Nano composites were determined using a highly sensitive photoacoustic (PA) technique. All the determined results were used for explaining how changing the percentages of CuO (NP_s) can dramatically affect the thermal and optical parameters that can be used for improving the seawater desalination technology. Therefore, synthesis of our CuO/Fe_3O_4 can be an effective (NCs) to overcome some of the technical problems in wastewater treatment techniques.

2. Experimental work

2.1. Materials

Fe_3O_4 (NPs) was prepared by using ferric chloride hexa-hydrate ($FeCl_3{\cdot}6H_2O$) and ferrous chloride tetra-hydrate ($FeCl_2{\cdot}4H_2O$), while the CuO (NPs) was produced from ammonium solution (26 % of ammonia) from Analar (England). acetone from Molar Hungary); and nitrogen gas (N_2) with 99.9 % purity, after that, they were mixed with an appropriate quantity of copper chloride ($CuCl_2$) and copper nitrate (Cu (NO_3) $2.3H_2O$) from India. Sodium hydroxide NaOH (pellets) was purchased from Lobha Chemie. Deionized water was used during the experimental preparations.

2.2. Fe_3O_4 (NPs), CuO (NPs) and CuO/Fe_3O_4 synthesis

The overall process for preparing Fe_3O_4 (NPs) was reported in our previous paper [31], while the CuO (NPs) was produced from ammonium solutions, acetone, nitrogen gas and were mixed with copper chloride and copper nitrate [32,33]. As for the preparation of CuO/-Fe_3O_4 nanocomposite, different percentages of powder prepared for the previous nanometers CuO NPs and Fe_3O_4 NPs are taken and placed in a mill, and were milled with fixed percentage of (0, 0.5, 0.6, 0.7, 0.8, 0.9, 1 wt%) of CuO NPs into Fe_3O_4 (NPs) to get CuO/Fe_3 O_4 (NCs) as shown in Fig. 1.

Seawater desalination as seen in Fig. 1 shows how we remove salt and impurities from seawater to produce drinking water. The aim is to convert seawater into fresh water for drinking irrigation and other uses. The salts, however, do not disappear, they are instead concentrated. The salt water is heated, or the water is allowed to evaporate and the water vapor is collected and condensed to form pure fresh water, and salt is left behind and can be used for other purposes.

2.3. The measurements tool

The X-ray diffraction (Rigaku, Miniflix 600) was utilized to carry out the crystal structure of CuO (NPs), Fe_3O_4 (NPs) and CuO/Fe_3O_4 (NCs). To investigate the surface morphology and the elemental detection of CuO (NPs), Fe_3O_4 (NPs) and CuO/Fe_3O_4 (NCs), scanning electron microscope (SEM) (JOEL-JSM Model 5600) coupled with energy -dispersive X-ray spectroscopy (EDX) (Shim ADZU diffractometer type XRD 6000) was utilized. The particle size of the prepared samples was detected via transmission Electron microscope (TEM) (HRTEM, JEOL JEM-2100 operated at 200 KV with high resolution Gatan CCD bottom camera, Orius SC200). UV–visible absorption and transmittance were measured to determine the optical properties, in the wavelength range of 200–750 nm, by using (V-670 Jasco double-beam Spectrophotometer) at room temperature. A highly sensitive (PA) (MTEC Model 300) technique **was** used to investigate the thermal parameters. In addition, an optical fiber probe model (FOBS) immersed in the resulting solution and connected to digital meter model (OMEGA-FOB) was used for monitoring the performance of temperature of the resulting solution. A computer interface program is used for registering the temperature rise with time for the prepared samples.

3. Results and discussion

3.1. Synthesized and characterization

The XRD pattern for synthesized CuO (NPs), Fe_3O_4 (NPs), and CuO/

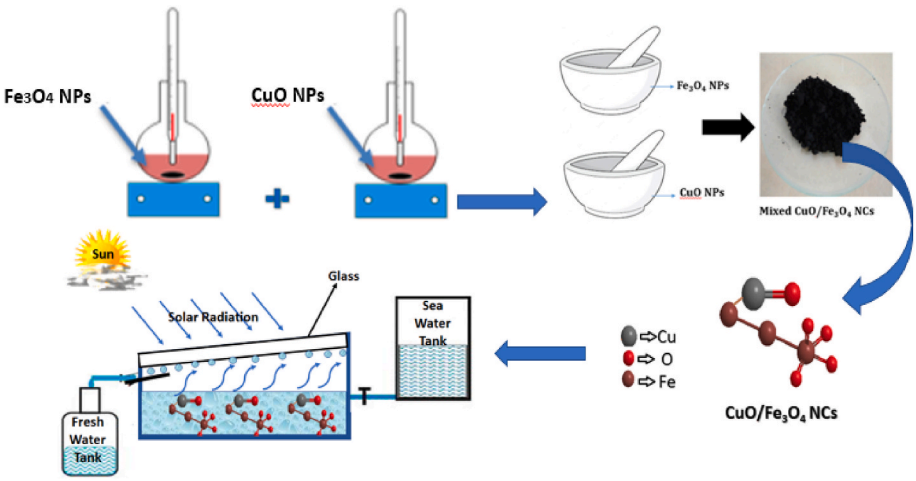

Fig. 1. The experimental steps used for the preparation of CuO/Fe_3O_4 (NCs).

Fe_3O_4 (NCs), are shown in Fig. 2 (a,b&c). The diffraction peaks at (220), (311), (400), (422), (511) and (440) seen in **Fig(a)** according to card number (JCPDS No. 88–0315) corresponding to pure Fe_3O_4 NPs [34–36].

While the observed peaks at (110), (002), (111), (202), (020), (113), (311),(220), (311) and (222) corresponding to CuO, in a good agreement with the standard JCPDS card number (JCPDS No. 89–2530) as seen in Fig. 2(b). In the case of Fig. 3(c) it is noticeable that the diffraction peaks obtained at (220), (311), (400) and (422) confirming the synthesis of CuO/Fe_3O_4 as recording in the standard card file No. (JCPDS No. 88–0315).

3.2. Surface morphological characteristics

The surface morphological study of 7%wt of CuO(NPs) in CuO/Fe_3O_4 (NCs) as a representative example was carried out using (SEM) micrograph images with different magnification resolutions as shown in Fig. 3 (a),while the EDX analyses,of the as-synthesized (NPs) depicts the presence of Fe, Co and O elements as seen in Fig. 3(b), that clearly indicating the purity of the as-synthesized (NPs) and confirm the existence of the chemical analysis observed in the (SEM) images.

The results reveal that CuO and Fe_3O_4 nanoparticles grew over the substrate surface, with doping 7 % of CuO NPs into Fe_3O_4 NPs. The elemental mapping seen in Fig. 3(c) analyzes and confirms the information of the distribution of the sample as previously seen in the SEM images and the EDX analysis as well. TEM is a powerful technique for understanding various information at very high spatial resolution such as sized particle, morphology crystal structure of materials.

The measured crystallite size of Fe_3O_4, Seen in Fig. 4(a) is 20 nm which agree with that calculated from XRD peaks by Scherer formula. Fig. 4 (b) shows the selected area electronic diffraction (SAED) of CuO (NPs), which indicates that the particles are well crystallized, and the diffraction rings on (SAED) image matches with the peaks in (XRD) pattern. Proving the monoclinic structure of as prepared CuO (NPs). In Fig. 4(c&d) the images revealed that, most (NPs) were in CuO/Fe_3O_4 (NCs),. The TEM images were consistent with the SEM images seen previously in Fig. 3.

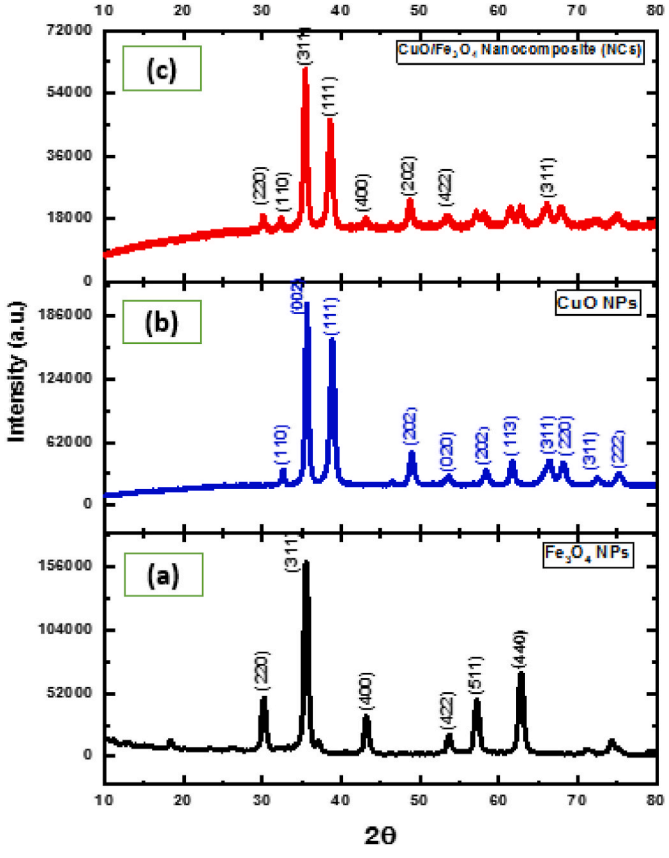

Fig. 2. XRD of **(a)** Fe_3O_4 NPs, **(b)** CuO NPs and **(c)** 0.7 wt % CuO/Fe_3O_4 (NCs) samples.

3.3. Optical characterization of CuO/Fe_3O_4 (NCs)

The spectral distribution of absorption and transmittance at room temperature for CuO/Fe_3O_4 (NCs) with various concentrations of CuO (NPs) is seen in Fig. 5(a&b).

It is obvious from Fig. 5(a&b) that, absorption and transmittance were affected by the change in the ratio of CuO %,where the absorption increase while the transmittance decrease with the increase of CuO (NPs) in CuO/Fe_3O_4 (NCs).The strong absorption peaks around 350–450 nm are due to the fundamental band gap. The absorption coefficient ***(α)*** is related to the absorbance ***(A)*** and the thickness ***(t)*** by the relation [37,38].

$$\alpha = 2.303\ A/t \tag{1}$$

The variation of ***(α)*** with ***(h ν)*** for CuO/Fe_3O_4 (NCs) with various ratios of CuO (NPs) is seen in Fig. 6.

It is clear from the evaluated values of the absorption coefficient given in Fig. 6 that the increase of the CuO(NPs) percent depending on the increase in ***(α)***, and reflected the modification occurred in CuO/Fe_3O_4 (NCs) samples band structure. The Urbach energy ***(E_U)***, can be estimated by extrapolating the straight line of the Urbach plot (ln α versus h ν) as given in Ref. [39] and seen in Fig. 7.

The Urbach empirical rule was confirmed by the straight-line fitting. The slope of the straight lines gives the value of ***(E_U)*** as observed in Table. 1. Using the Urbach energy values, one can define the broadening of the optical absorption edge which is based on the carrier interaction, the steepness parameter ***(σ)*** can be estimated in terms of ***(E_U)*** from the following form [39].

$$\sigma = \frac{K_B\ T}{E_U} \tag{2}$$

Where ***(k_B)*** is Boltzman constant, ***(T)*** is the absolute temperature in Kelvin. The value of the electron phonon interaction ***($E_{e\text{-}p}$)*** can be defined from the steepness parameter ***(σ)*** according to the following formula [39].

$$E_{e-p} = \frac{2}{3\sigma} \tag{3}$$

The estimated values of ***(σ)*** and ***($E_{e\text{-}p}$)*** versus CuO NPs concentration is given in Table 1. Fig. 8 show the variation of both ***(σ)*** and $E_{e\text{-}p}$ with different ratio of CuO in CuO/Fe_3O_4 (NCs).

It is obvious from Fig. 8, that the ***($E_{e\text{-}p}$)*** enhances while ***(σ)*** decreases with the increase of CuO (NPs) content. This behavior is evidence of the increase of the degree of ionicity of crystallographic bonds which is a result of the systematic analysis of the crystal structure given in 3.1 and 3.2.

The optical band gap **(E_g)** can be obtained from the optical absorption using Tauc's energy exponential relation [38]:

$$(ahv) = (hv - E_g)^r \tag{4}$$

where ***(α)*** is the absorption coefficient, ***(B)*** is a constant, ***(E_g)*** is the optical band gap, and the exponent ***(r)*** assumes values of 1/2, 2, 3/2 or 3 for allowed direct, allowed indirect, forbidden direct, and forbidden indirect transitions, respectively.

The direct optical band gaps were determined by extrapolating straight line till X-axis as is illustrated in Fig. 9(b). The effect adding CuO (NPs) into CuO/Fe_3O_4 NCs is very clear through the change that occurred in the direct energy gap values ***(E_g)*** as seen in Fig. 9 and

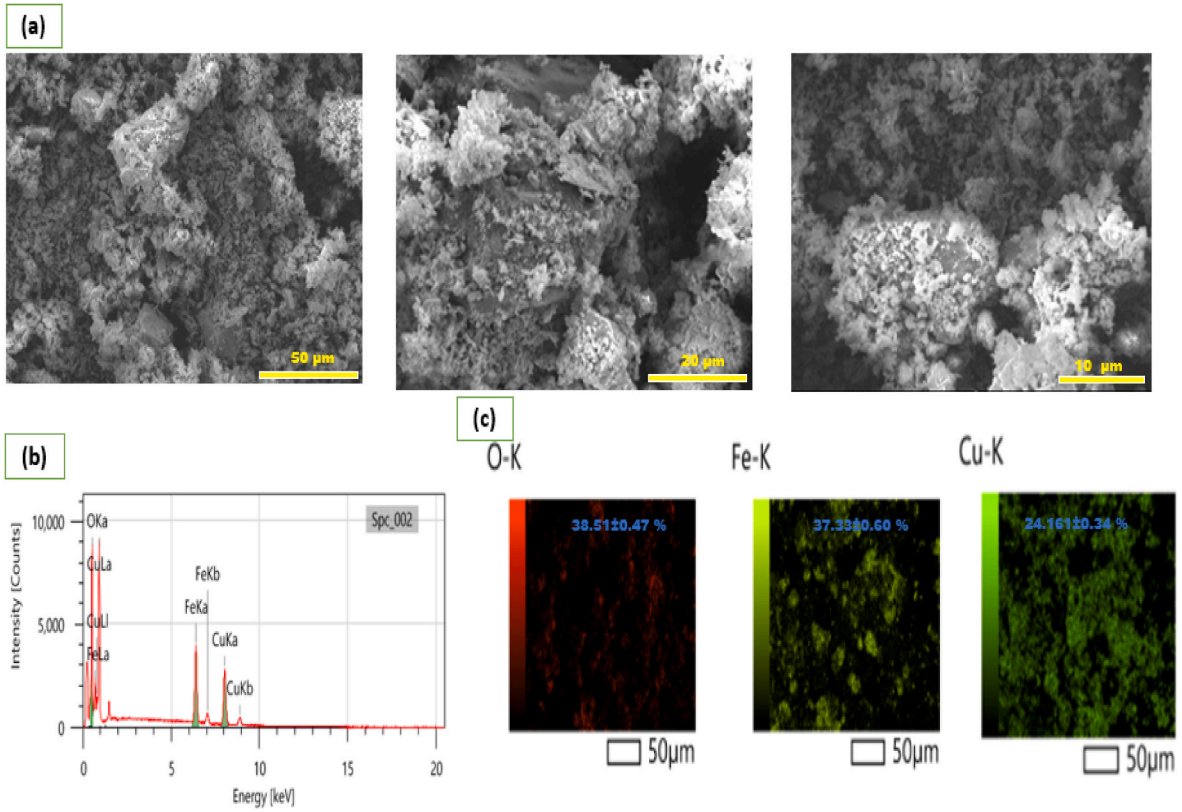

Fig. 3. (a), (b), (c) present the SEM fracture surface samples, EDX analysis and mapping for 0.7 wt % CuO/Fe_3O_4 NCs respectively.

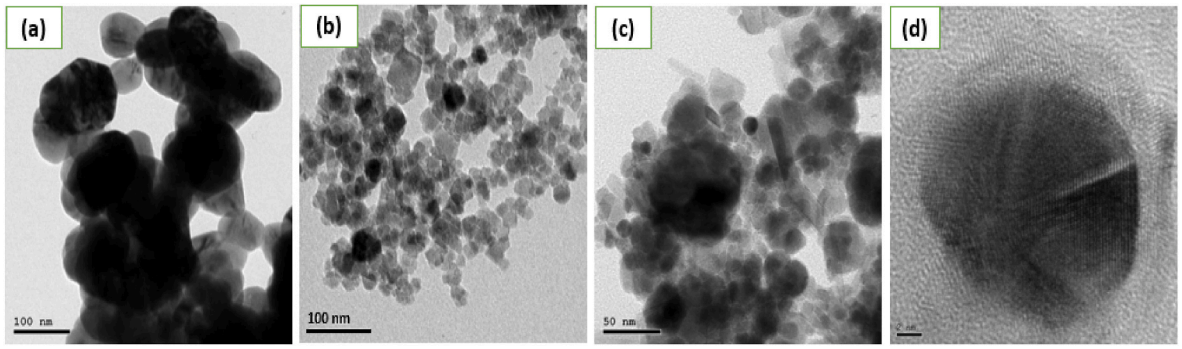

Fig. 4. (a), (b) presents the TEM image analysis for CuO NPs and Fe_3O_4 NPs respectively, **(c)** and **(d)** Present the TEM image for 0.7 wt % CuO/Fe_3O_4 NCs with different resolution.

Table .2.The (E_g) values decreased from 2.52 to 2.15 eV with increasing the CuO content from (0.0–1.0 wt%) in CuO/Fe_3O_4 (NCs) which based on the change in the network structure and is an indication that the incorporation of CuO (NPs) has a tendency to disperse the energy states between valence band and conduction band [40]. The further decrease in (E_g) with the addition of CuO (NPs) wt%, allowed states to well merge with the conduction band resulting in the reduction of the band gap. The shrinkage in the optical gap of the NCs films is attributed to created localized energetic states due to CuO filling between energetic bands of the host Fe_eO_4 NPs. It is obvious that the obtained optical band gap of the prepared films from the absorption data and Tauc´s method are well compatible as well as with the reported ones, and can be attributed also to the improvement in crystal morphological changes seen in XRD, SEM, and TEM. The inverse relation between (E_g) and (E_U) was found as expected with increasing CuO (NPs) content in CuO/Fe_3O_4 (NCs) as seen in Fig. 10, which means that when having narrower bandgap, it is expected to have a wider band tail.

To evaluate the optical properties for any application it is necessary to do research on the refractive index (n). The refractive indices (n) was calculated based on the optical energy gap by using three different equations [41]:

$$n^4 E_g = 95eV \tag{5}$$

$$n = k\left[E_g\right]^C \tag{6}$$

$$n^2 = 1 + \left[\frac{A}{E_g + B}\right]^2 \tag{7}$$

where K = 3.3668, C = −0.32234, A = 13.6 eV and B = 3.47 eV. According to the above relation the refractive index **(n)** was determined and tabulated in Table 02.

As can be seen from Table 2, that the (n_{av}) estimated from n_5, n_6 and n_7 given from equations (5)–(7) respectively,increased from 2.48 to 2.58

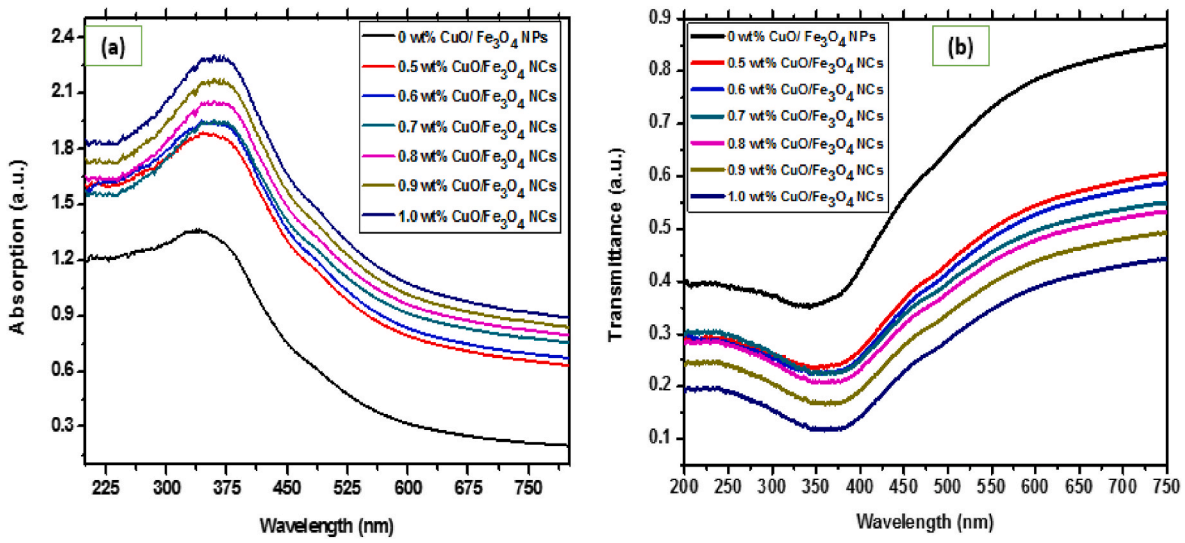

Fig. 5. (a&b) Absorption and transmittance spectra for different concentration of CuO (NPs) in CuO/Fe_3O_4(NCs).

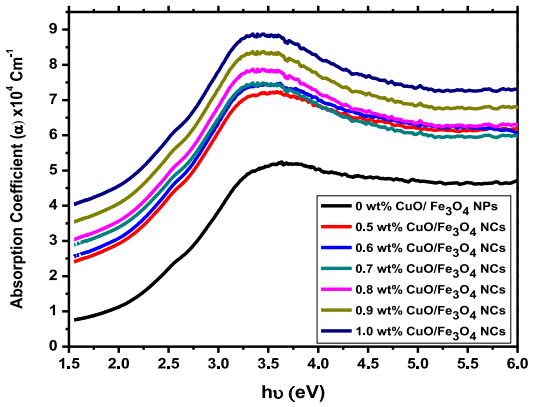

Fig. 6. Variation of (α) versus (h ν) for different CuO/Fe_3O_4 (NCs).

Table 1
Urbach energy (E_U), Steepness parameter (σ), Electron-Phonon interaction ($E_{e\text{-}p}$) for different ratios of CuO NPs on CuO/Fe_3O_4 NCs.

Samples	Urbach energy (E_U) (eV)	Steepness parameter (σ) x10^{-3} (eV)	Electron-Phonon interaction ($E_{e\text{-}p}$)
0 wt% CuO/ Fe_3O_4 NCs	**1.28**	**18**	**36.29**
0.5 wt% CuO/ Fe_3O_4 NCs	**1.36**	**17**	**38.75**
0.6 wt% CuO/ Fe_3O_4 NCs	**1.48**	**16**	**42.19**
0.7 wt% CuO/ Fe_3O_4 NCs	**1.63**	**15**	**46.29**
0.8 wt% CuO/ Fe_3O_4 NCs	**1.74**	**14**	**49.38**
0.9 wt% CuO/ Fe_3O_4 NCs	**1.97**	**12**	**56.02**
1.0 wt% CuO/ Fe_3O_4 NCs	**2.2**	**11**	**62.89**

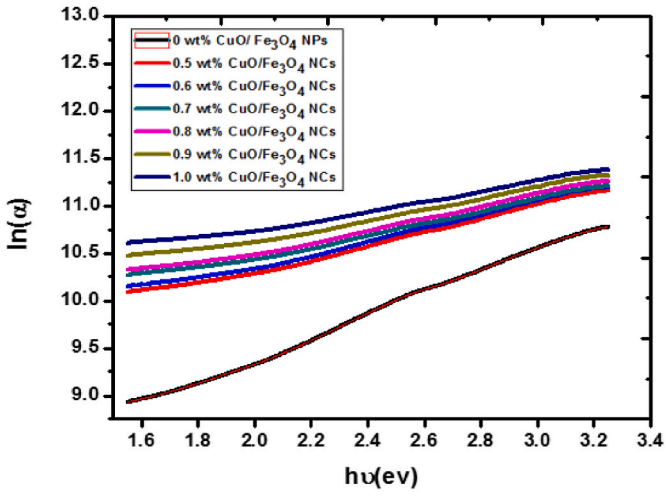

Fig. 7. Dependence of (lnα) of CuO/Fe_3O_4 (NCs) with various concentration of CuO (NPs) upon (h ν).

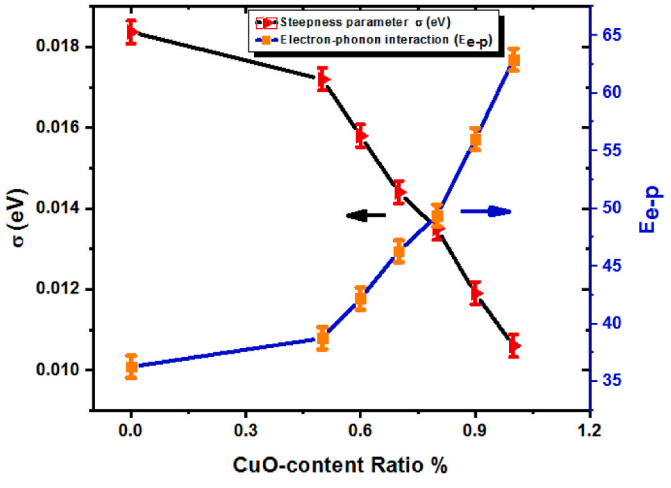

Fig. 8. Dependence of both (σ) and $E_{e\text{-}p}$ of different percent of CuO % in CuO/Fe_3O_4 NCs.

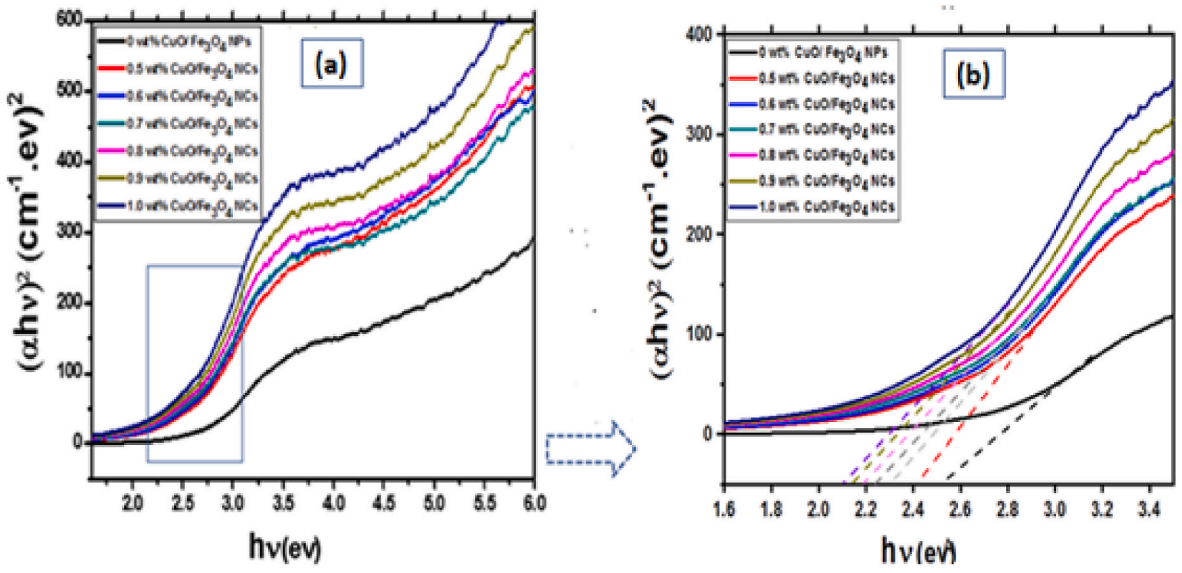

Fig. 9. (a&b) plot of $(\alpha h \upsilon)^2$ versus $(h \upsilon)$ with different scales for CuO/Fe_3O_4 NCs as a function of CuO at %.

Table 2
Values of **(E_g), (n)** for different ratios of CuO NPs in CuO/Fe_3O_4 NCs.

Samples	Energy gap (E_g) (eV)	Refractive index n_5 n_6 n_7 n_{av}			
0 wt% CuO/Fe_3O_4 NCs	**2.52**	**2.47**	**2.49**	**2.50**	**2.48**
0.5 wt% CuO/Fe_3O_4 NCs	**2.42**	**2.50**	**2.53**	**2.51**	**2.51**
0.6 wt% CuO/Fe_3O_4 NCs	**2.34**	**2.52**	**2.55**	**2.52**	**2.53**
0.7 wt% CuO/Fe_3O_4 NCs	**2.31**	**2.53**	**2.57**	**2.53**	**2.54**
0.8 wt% CuO/Fe_3O_4 NCs	**2.29**	**2.54**	**2.58**	**2.54**	**2.55**
0.9 wt% CuO/Fe_3O_4 NCs	**2.23**	**2.55**	**2.59**	**2.55**	**2.56**
1.0 wt% CuO/Fe_3O_4 NCs	**2.15**	**2.57**	**2.63**	**2.56**	**2.58**

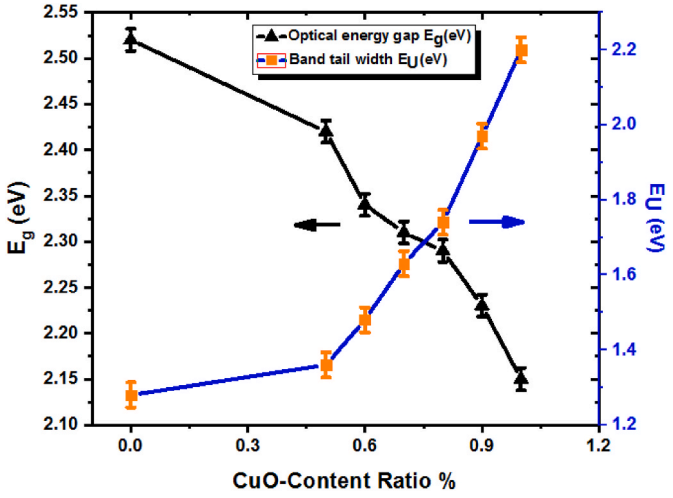

Fig. 10. Dependence of (E_g) and (E_u) versus different ratios of CuO%.

with increasing the CuO content in CuO/Fe_3O_4 (NCs). Optical conductivity ***(σ_{opt})***,is an additional essential optical parameter that can be detected from the value of ***(n_{av})*** according to the relation [42].

$$\sigma_{opt} = \frac{\alpha \; n_{av} \; c}{4\pi} \tag{8}$$

Where (α) is the absorption coefficient, ***(n_{av})*** is the refractive index and ***(c)*** is the speed of light in air ($3x10^8$ m/s). It is seen from Fig. 11 that the values of ***(σ_{opt})*** increase with increasing CuO content in CuO/Fe_3O_4 (NCs). The observed improvement in the optical conductivity that has

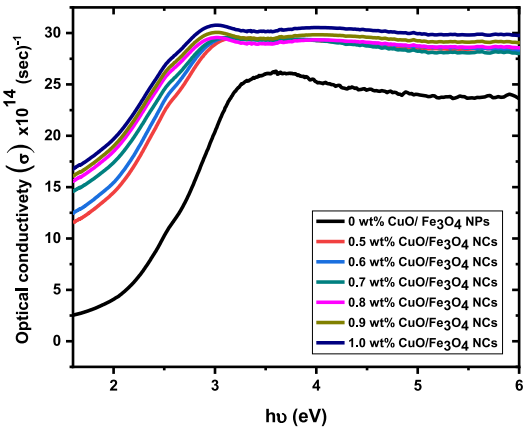

Fig. 11. (σ_{opt}) versus ($h\nu$) plot for different concentration of CuO NPs in CuO/Fe_3O_4 NCs.

occurred is the result of the increase in the absorption (seen in Fig. 6), and in the concentration of the charge carriers that occurs in CuO/Fe_3O_4 (NCs) with the increasing of CuO (NPs) percent. Furthermore, the inversely proportional relation between the optical conductivity and the optical energy gap is also confirmed by comparing Fig. 9 with Fig. 11.

3.4. The desalination performance of Fe_3O_4 (NPs)

Reducing the fresh water sources with the global growing, and the demand for drinking water is increasing, therefore desalination could be a reliable solution to the shortage of potable water scarcity by help preserve habitats reliant on those same water resources. The Photo-acoustic (PA) thermal characterization technique, was utilized to know the thermodynamics of the adsorption process of the liquid samples of Fe_3O_4 (NPs) and CuO/Fe_3O_4 (NCs) in seawater as seen in Fig. 12 (a). The performed analysis of the PA amplitude ***(q)*** and frequency ***(f)*** indicates the adsorption process based on the following formula [31]:

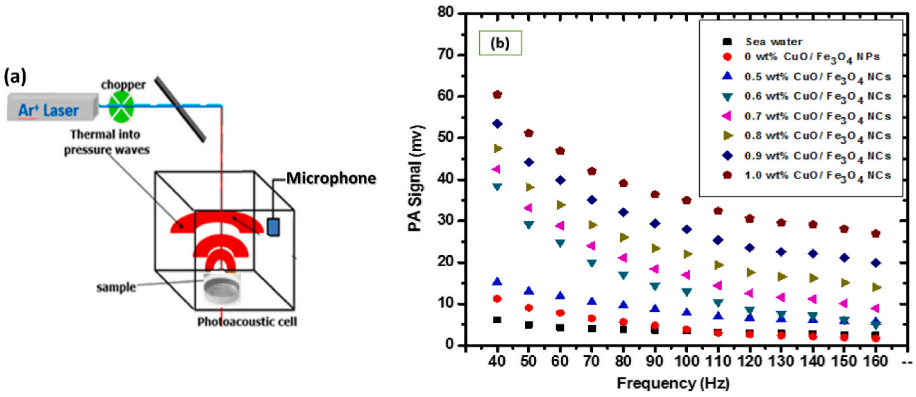

Fig. 12. Plots of (PA) **(a)** for set-up diagram for thermal measurements, **(b)** for (q) versus (f) for the prepared samples.

$$q = \frac{A\beta\mu_s}{2\pi f e\sqrt{(\ \beta\mu_s + 1\ )^2 + 1}}, \mu_s = \left(\frac{D_{th}}{\pi f}\right)^{\frac{1}{2}} \tag{9}$$

Where (β) is the optical absorption coefficient, ***(e)*** is sample thermal effusivity, (μ_s) is thermal diffusion length and (***A***) is constant (not related to the sample). The results of the desalination dependent behavior are shown in Fig. 12 (b) for signal amplitude (***q***) versus (***f***). Both the thermal diffusivity (D_{th}), effusivity ***(e)*** were evaluated from the fitting of Fig. 12 [31]. The thermal transport properties can also be determined via the thermal conductivity (K) that can be correlated by Ref. [31].

$$K = e\sqrt{D_{th}} \tag{10}$$

From Table 3, as can be seen, the increase in (***K***) of Fe_3O_4 NPs values with increasing the CuO (NPs) percent in the CuO/Fe_3O_4 NCs, is an indication of the presence of the localized surface plasmon resonance. A noticeable agreement is also observed with the results of the optical conductivity ***(σ_{opt})*** given in Fig.(11), confirming the incorporation of CuO (NPs) with the Fe_3O_4(NPs). In addition, the results showed that the CuO/Fe_3O_4(NCs) is better than Fe_3O_4(NP_S) in enhancing the strength in driving force. This was due to the improvement of thermal conductivity as illustrated in Table 3,. The measurements were defined by using surfactant (Triton X-100), into the water-based Fe_3O_4 NPs and CuO/Fe_3O_4 NCs that were ultrasonically dispersed in seawater [31].

A solar simulator xenon lamp with (200Watt and irradiance (1000W/m^2) estimated by power meter at various duration time of (60) minutes was used for determining the photo-thermal conversion characteristics as shown in Fig.13 (a). An increase of the nanofluid temperature is depicted in Fig13 (b). The observed variation in the initially proposed temperature indicates that the photo-thermal conversion efficiency, of CuO/Fe_3O_4 (NCs) are quantified by the increase of CuO percent, and by the strong absorption as well as the capturing of solar radiation.

3.5. Coefficient performance of thermal efficiency

Thermal efficiency quantifies the percentage of heat used for evaporation, The effect of different concentration of CuO (NPs)in CuO/Fe_3O_4 (NCs) on the thermal efficiency of seawater desalination., can be utilized by using the photo-thermal conversion efficiency (η) *that* can be estimated by the following equation [43–45].

$$\eta = \frac{\Delta T c_w m_w}{\Delta t A G} \times 100\% \tag{11}$$

Where, (c_w) and (m_w) are the specific heat and the mass of the water, respectively, (ΔT) is the temperature difference of the nanofluid after an exposed time (Δt); (A) is the irradiation area; (G) (W m^{-2}) is the irradiation intensity Furthermore, The (NPs) temperature measured by the thermocouple, appeared to be the same as the temperature of the surrounding fluid. This conclusively demonstrates that the depth of the fluid is small, and confirms the uniform of the solar radiation. An observed increase in the efficiency by adding the surfactant (Triton X-100) to Fe_3O_4 NPs and CuO/Fe_3O_4 NCs is depicted in Fig. 13 (c), were the presence of nanoparticle suspended in seawater increases the absorption (direct absorption) of incident radiation more than that of pure seawater, upon adding CuO(NPs), which is an indication of the increase of heating efficiency. As we know the volumetric absorption process addresses the limitation of the surface heat transfer, which is normally associated with the improvement in the conversion efficiency. The change in the absorption spectra is directly linked to the photo-thermal efficiency. This observation reflects the modifications that had been occurred with the surface plasmons results, as well as the increase of the absorption and thermal conductivity. Moreover, a good agreement can be seen when comparing with the (n_{av}) values given in Table 2, with the given data presented in Table 3, where a higher temperature means the liquid becomes less dense causing light to travel faster in the medium.

4. Conclusions

The interplay between CuO/Fe_3O_4 (NCs) and CuO (NPs) have been verified and summarized in the above study. Findings from X-ray, SEM, EDX, and TEM, show that adding CuO (NPs) To CuO/Fe_3O_4 (NCs) demonstrate a noticeable difference in the microstructures and morphology of synthesized nanocomposites. The incorporation of CuO (NPs) into Fe_3O_4 (NPs) led to an increase in absorption coefficient (α), Urbach energy (E_U), refractive index (n), Thermal conductivity (k) and thermal efficiency (η) while a decrease in the transmittance (T) and the optical energy gap (E_g) was observed. Furthermore, the influence CuO (NPs) concentration on of thermal effusivety and thermal diffusivity was discussed, and proved the effect of solar thermal desalination on the freshwater production. From this analysis, our results show a strong dependence and correlation between the increase in CuO (NPs) into Fe_3O_4 (NPs) and the above mention parameters, and therefore maybe it is 'an indication of the increase in desalination process efficiency in future roadmap.

CRediT authorship contribution statement

S.S. Fouad: Writing – review & editing, Writing – original draft, Formal analysis, Data curation, Conceptualization. **M. Nabil:** Writing – review & editing, Writing – original draft, Investigation, Funding acquisition, Formal analysis, Data curation, Conceptualization. **F. Horia:** Writing – original draft, Funding acquisition, Formal analysis, Data curation, Conceptualization. **K. Easawi:** Writing – review & editing, Writing – original draft, Conceptualization. **S. Negm:** Writing – original draft.

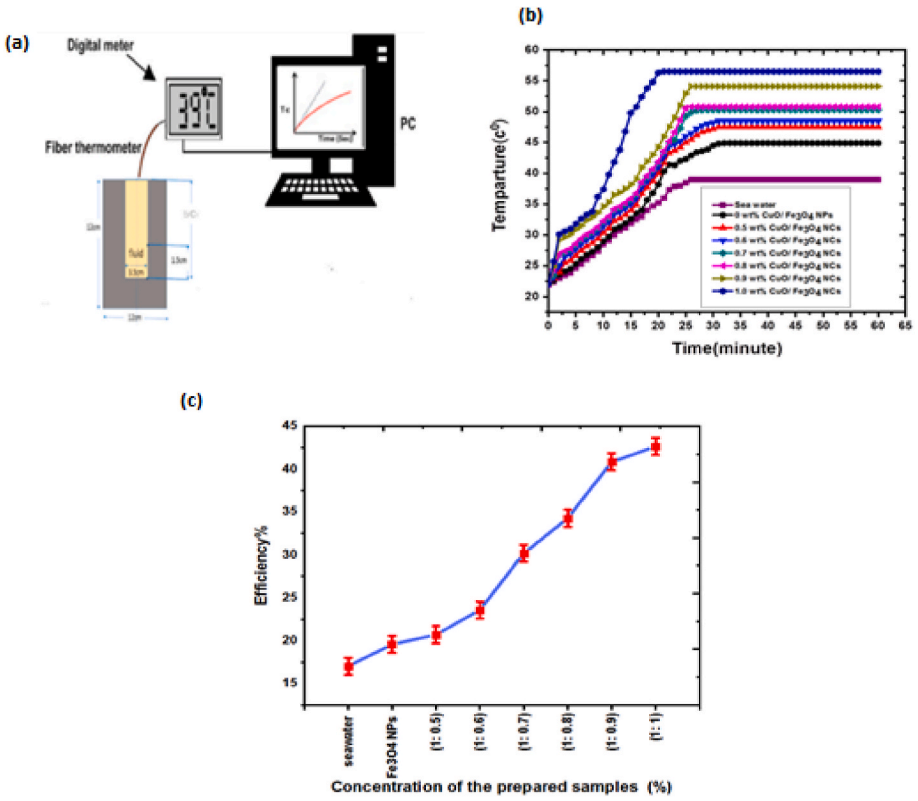

Fig. 13. (a) Experimental illustration of the variation of temperature rise with time. (b) The temperature distribution with time (c) Photo-thermal conversion efficiency for in CuO/Fe_3O_4 NCs.

Table 3
The diffusivity, effusivity and the conductivity in CuO/Fe_3O_4 (NCs).

Samples	Diffusivity (α) $x10^{-3}$ Cm^2/Sec	Effusivity (e) $WSec^{1/2}$ $Cm^{-2}K^{-1}$	Conductivity (K) $x10^{-3}$ W/Cm.K
Seawater	**1.38**	**0.15**	**5.76**
0 wt% CuO/ Fe_3O_4 NCs	**1.50**	**0.17**	**6.62**
0.5 wt% CuO/ Fe_3O_4 NCs	**1.55**	**0.18**	**6.96**
0.6 wt% CuO/ Fe_3O_4 NCs	**1.61**	**0.18**	**7.24**
0.7 wt% CuO/ Fe_3O_4 NCs	**1.65**	**0.19**	**7.62**
0.8 wt% CuO/ Fe_3O_4 NCs	**1.74**	**0.20**	**8.17**
0.9 wt% CuO/ Fe_3O_4 NCs	**1.86**	**0.21**	**8.76**
1.0 wt% CuO/ Fe_3O_4 NCs	**1.94**	**0.22**	**9.59**

Declaration of competing interest

I and all the authors declare that we do not have known competing financial interests or personal relationships that may have affected the work mentioned in this paper.

References

[1] Madhavi Dahanayaka, Bo Liu, Narasimalu Srikanth, Kun Zhou, "Ionised graphene oxide membranes for seawater desalination.", Desalination 496 (2020) 114637.
[2] Meysam Faegh, Mohammad Behshad Shafii, Thermal performance assessment of an evaporative condenser-based combined heat pump and humidification-dehumidification desalination system, Desalination 496 (2020) 114733.
[3] William Toh, Elisa YM. Ang, Teng Yong Ng, Rongming Lin, Zishun Liu, An investigation on the effects of nanoplastic particles on nanoporous graphene membrane desalination, Desalination 496 (2020) 114765.
[4] Yang Xu, Feng Duan, Yuping Li, Hongbin Cao, Junjun Chang, Haoliang Pang, Jianxin Chen, Enhanced desalination performance in asymmetric flow electrode capacitive deionization with nickel hexacyano ferrate and activated carbon electrodes, Desalination 514 (2021) 115172.
[5] K. Ulbrich, K. Hola, V. Subr, A. Bakandritsos, J. Tucek, R. Zboril, Targeted drug delivery with polymers and magnetic nanoparticles: covalent and noncovalent approaches, release control, and clinical studies, Chem. Rev. 116 (2016) 5338–5431.
[6] A. Mishra, K and Ramaprabhu S Nano magnetite decorated multiwalled carbon nanotubes: a robust nanomaterial for enhanced carbon dioxide adsorption *Energy Environ. Sci* 4 (2011) 889–895.
[7] D.H.K. Reddy, Y.S. Yun, Spinel ferrite magnetic adsorbents: alternative future materials for water purification, Coord. Chem. Rev 315 (2016) 90–111.
[8] K.K. Kefeni, B.B. Mamba, T.A.M. Msagati, Application of spinel ferrite nanoparticles in water and wastewater treatment: a review, Sep. Purif. Technol. 188 (2017) 399–422.
[9] J. Gómez-Pastora, E. Bringas, I. Ortiz, Recent progress and future challenges on the use of high-performance magnetic nano-adsorbents in environmental applications, Biochem. Eng. J. 256 (2014) 187–204.
[10] J. Gómez-Pastora, S. Dominguez, E. Bringas, et al., Review and perspectives on the use of magnetic nanophotocatalysts (MNPCs) in water treatment, Chem. Eng. J. 310 (2016) 407–427.
[11] I. Karimzadeh, M. Aghazadeh, M.R. Ganjali, P. Norouzi, T. Doroudi, P.H. Kolivand, Electrochemical deposition (CED) saccharide-coated super paramagnetic Fe_3O_4 nanoparticles (SPIONs) for biomedical applications: an efficient and scalable route for preparation and in situ surface coating through cathodic Mater. Lett 189 (2017) 290–294.
[12] D. Ling, N. Lee, T. Hyeon, Chemical synthesis and assembly of uniformly sized iron oxide nanoparticles for medical applications Acc. Chem. Res 48 (2015) 1276–1285.
[13] K. Ulbrich, K. Hola, V. Subr, A. Bakandritsos, J. Tucek, R. Zboril, Targeted drug delivery with polymers and magnetic nanoparticles: covalent and noncovalent approaches, release control, and clinical studies, Chem. Rev. 116 (2016) 5338–5431.
[14] A.K. Mishra, S. Ramaprabhu, Nano magnetite decorated multiwalled carbon nanotubes: a robust nanomaterial for enhanced carbon dioxide adsorption Energy Environ. Sci 4 (2011) 889–895.
[15] J. Hu, H. Wang, F. Dongc, Z. Wu, A new strategy for utilization of NIR from solar energy—promotion effect generated from photo-thermal effect of Fe_3O_4@SiO_2 for photocatalytic oxidation of NO, Appl. Catal., B 204 (2017) 584–592.

[16] K. Yang, S. Zhang, G. Zhang, X. Sun, S.T. Lee, Z. Liu, Graphene in mice: ultrahigh in vivo tumor uptake and efficient photothermal therapy, Nano Lett. 10 (2010) 3318–3323.
[17] X. Huang, I.H. El-Sayed, W. Qian, M.A. El-Sayed, Cancer cell imaging and photothermal therapy in the near-infrared region by using gold nanorods J. Am. Chem. Soc 128 (2006) 2115–2120.
[18] Q. Chen, H. Ke, Z. Dai, Z. Liu, Nanoscale theranostics for physical stimulus-responsive cancer therapies, Biomaterials 73 (2015) 214–230.
[19] A.S. Lanje, R.S. Ningthoujam, S.J. Shrama, R.K. Vatsa, R.B. Pode, Int. J. Nanotechnol. 7 (2010) 979.
[20] E.P. Wolhfarth, Ferromagnetic Materials, II, 1980. North-Holland, Amsterdam, New York, Oxford, Tokyo.
[21] Tsuneo Mitsuyu, Osamu Yamazaki, Kenzo Ohji, Kiyotaka Wasa, Piezoelectric thin films of zinc oxide for saw devices, Ferroelectrics 42 (1) (1982) 233–240.
[22] Laurence M. Peter, The gratzel cell: where next? J. Phys. Chem. Lett. 2 (15) (2011) 1861–1867.
[23] Amrut S. Lanje, Satish J. Sharma, Ramchandara B. Pode, Raghumani S. Ningthoujam, Synthesis and optical characterization of copper oxide nanoparticles, Adv. Appl. Sci. Res. 1 (2) (2010) 36–40.
[24] Ulrika Bjoerksten, Jacques Moser, Michael Graetzel, Photoelectrochemical studies on nanocrystalline hematite films, Chem. Mater. 6 (6) (1994) 858–863.
[25] Wei-Ping Dow, Ta-Jen Huang, Yttria-stabilized zirconia supported copper oxide catalyst: II. Effect of oxygen vacancy of support on catalytic activity for CO oxidation, J. Catal. 160 (2) (1996) 171–182.
[26] Per-Olof Larsson, Arne Andersson, L. Reine Wallenberg, Bo Svensson, Combustion of CO and toluene; characterization of copper oxide supported on titania and activity comparisons with supported cobalt, iron, and manganese oxide, J. Catal. 163 (2) (1996) 279–293.
[27] Yan Jiang, Shawn Decker, Cathy Mohs, Kenneth J. Klabunde, Catalytic solid-state reactions on the surface of nanoscale metal oxide particles, J. Catal. 180 (1) (1998) 24–35.
[28] S. Lee, S. Su-S Choi, Li, J.A. Eastman, Measuring Thermal Conductivity of Fluids Containing Oxide Nanoparticles, 1999, pp. 280–289.
[29] J.F. Xu, W. Ji, Z.X. Shen, W.S. Li, S.H. Tang, X.R. Ye, D.Z. Jia, X.Q. Xin, Raman spectra of CuO nanocrystals, J. Raman Spectrosc. 30 (5) (1999) 413–415.
[30] K. Manmeet, K.P. Muthea, S.K. Despandeb, Ch Shipra, J.B. Singhd, V. Neetika, S. K. Gupta, J.V. Yakhmi, Growth and branching of CuO nanowires by thermal oxidation of copper, J. Cryst. Growth 289 (2011) 670–675.
[31] M. Nabil, S.S. Fouad, K. Easawi, S. Abdallah, F. Horia, Novel correlations between optical absorption and water desalination of Ag/Fe_3O_4 Nanocomposite prepared by pulsed laser ablation, Opt Laser. Technol. 164 (2023) 109545.
[32] W. Narongdet, C. Piyanut, V. Naratip, P. Wisanu, Sonochemical synthesis and characterization of copper oxide nanoparticles, Energy Proc. 29 (2011) 404–409.
[33] M.H. Yamukyan, K.V. Manukyan, S.L. Kharatyan, Copper oxide reduction by combined reducers under the combustion mode, Chem 137 (2008) 636–642.
[34] J. Zhu, D. Li, H. Chen, X. Yang, L. Lu, X. Wang, Highly dispersed CuO nanoparticles prepared by a novel quick-precipitation method, Mater. Lett. 58 (2004) 3324–3327.
[35] L. Sophie, F. Delphine, P. Marc, R. Alain, R. Caroline, V.E. Luce, N.M. Robert, Magnetic iron oxide nanoparticles: synthesis, stabilization, vectorization, physicochemical characterization, and biological applications, Chem. Rev. 108 (2008) 2064–2110.
[36] L. Ao, X. Hu, M. Xu, Q. Zhang, L. Huang, Central-radial bi-porous nanocatalysts with accessible high unit loading and robust magnetic recyclability for 4-nitrophenol reduction, Dalton Trans. 49 (2020) 4669–4674.
[37] S.S. Fouad, B. Parditka, A.E. Bekheet, H.E. Atyia, Z. Erdélyi, ALD of TiO_2/ZnO mutilayers towards the understanding of optical properties and polarizability, Opt Laser. Technol. 140 (2021) 107035.
[38] M. Nabil, Shaimaa A. Mohamed, K. Easawi, Salah SA. Obayya, S. Negm, H. Talaat, M.K. El-Mansy, Surface modification of CdSe nanocrystals: application to polymer solar cell, Curr. Appl. Phys. 20 (3) (2020) 470–476.
[39] I.M. El Radaf, H.Y.S. Al-Zahrani, S.S. Fouad, M.S. El-Bana, Profound optical analysis for novel amorphous Cu_2FeSnS_4 thin films as an absorber layer for thin film solar cells, Ceram. Int. 46 (11) (2020) 18778–18784.
[40] S.S. Fouad, G.B. Sakr, I.S. Yahia, D.M. Abdel Basset, Structural characterization and novel optical properties of defect chalcopyrite $ZnGa_2Te_4$ thin films, Mater. Res. Bull. 46 (11) (2011) 2141–2146.
[41] S.S. Fouad, M. Nabil, B. Parditka, A.M. Ismail, E. Baradács, H.E. Atyia, Zoltán Erdélyi. Assessing, surface morphology, optical, and electrical performance of ZnO thin ilm using ALD technique, Journal of nanoparticles research 25 (2023) 172.
[42] S.S. Fouad, Bence Parditka, M. Nabil, Eszter Baradács, S. Negm, Zoltán Erdélyi, Effect of Cu interlayer on opto-electrical parameters of ZnO thin films, J. Mater. Sci. Mater. Electron. 33 (26) (2022) 20594–20603.
[43] Yang Yung-Jih, David S. Corti, Elias I. Franses, Effect of Triton X-100 on the stability of titania nanoparticles against agglomeration and sedimentation: a masked depletion interaction, Colloids Surf. A Physicochem. Eng. Asp. 516 (2017) 296–304.
[44] Muhammad Wakil Shahzad, Muhammad Burhan, Doskhan Ybyraiymkul, Kim Choon Ng, Desalination processes' efficiency and future roadmap, Entropy 21 (1) (2019) 84.
[45] Hui Zhang, Hui-Jiuan Chen, Xiaoze Du, Dongsheng Wen, Photothermal conversion characteristics of gold nanoparticle dispersions, Sol. Energy 100 (2014) 141–147.